ADVANCED FUNCTIONAL MATERIALS
www.afm-journal.de

Halide Perovskites: Advanced Photovoltaic Materials Empowered by a Unique Bonding Mechanism

Matthias Wuttig, Carl-Friedrich Schön, Mathias Schumacher, John Robertson, Pavlo Golub, Eric Bousquet, Carlo Gatti, and Jean-Yves Raty*

Outstanding photovoltaic (PV) materials combine a set of advantageous properties including large optical absorption and high charge carrier mobility, facilitated by small effective masses. Halide perovskites (ABX_3, where X = I, Br, or Cl) are among the most promising PV materials. Their optoelectronic properties are governed by the B—X bond, which is responsible for the pronounced optical absorption and the small effective masses of the charge carriers. These properties are frequently attributed to the ns^2 configuration of the B atom, i.e., Pb $6s^2$ or Sn $5s^2$ ("lone-pair") states. The analysis of the PV properties in conjunction with a quantum-chemical bond analysis reveals a different scenario. The B—X bond differs significantly from ionic, metallic, or conventional 2c—2e covalent bonds. Instead it is better regarded as metavalent, since it shares about one p-electron between adjacent atoms. The resulting σ-bond, formally a 2c—1e bond, is half-filled, causing pronounced optical absorption. Electron transfer between B and X atoms and lattice distortions open a moderate bandgap resulting in charge carriers with small effective masses. Hence, metavalent bonding explains favorable PV properties of halide perovskites, as summarized in a map for different bond types, which provides a blueprint to design PV materials.

1. Introduction

Halide perovskites promise exceptional performance in optoelectronic applications ranging from inexpensive, high-performance photovoltaic (PV) modules[1–6] to light-emitting and lasing devices.[7–9] These perovskites display a rare combination of properties including pronounced optical absorption in conjunction with relatively large charge-carrier mobilities. Yet, they possess soft crystalline lattices with dynamic disorder.[10] Such a combination of properties is neither found in isostructural oxide perovskites nor in sp^3-bonded semiconductors. The remarkable properties of halide perovskites, which enable their application potential,[11–13] are frequently attributed to the impact of the divalent B cation. Specifically, the presence of $6s^2$ ($5s^2$) lone-pair electrons of Pb (Sn) is invoked to explain

M. Wuttig, C.-F. Schön
I. Institute of Physics
Physics of Novel Materials
RWTH Aachen University
52056 Aachen, Germany
E-mail: wuttig@physik.rwth-aachen.de

M. Wuttig
Jülich-Aachen Research Alliance (JARA FIT and JARA HPC)
RWTH Aachen University
52056 Aachen, Germany

M. Wuttig
PGI 10 (Green IT)
Forschungszentrum Jülich GmbH
52428 Jülich, Germany

M. Schumacher
Institute for Theoretical Solid State Physics
RWTH Aachen University
52056 Aachen, Germany

The ORCID identification number(s) for the author(s) of this article can be found under https://doi.org/10.1002/adfm.202110166.

© 2021 The Authors. Advanced Functional Materials published by Wiley-VCH GmbH. This is an open access article under the terms of the Creative Commons Attribution-NonCommercial License, which permits use, distribution and reproduction in any medium, provided the original work is properly cited and is not used for commercial purposes.

DOI: 10.1002/adfm.202110166

J. Robertson
Engineering Department
Cambridge University
Cambridge CB3 0FA, UK

P. Golub
Department of Theoretical Chemistry
J. Heyrovský Institute of Physical Chemistry
Dolejškova 2155/3, 182 23 Prague 8, Czech Republic

E. Bousquet
Physique Théorique des Matériaux
Q-MAT
CESAM
Université de Liège
Sart-Tilman B4000, Belgium

C. Gatti
CNR-SCITEC
Istituto di Scienze e Tecnologie Chimiche "Giulio Natta,"
Sezione di via Golgi, via Golgi 19, Milano 20133, Italy

J.-Y. Raty
CESAM B5
Université de Liège
Sart-Tilman B4000, Belgium

the PV properties.[14] Here we demonstrate that the unique property portfolio of halide perovskites is instead empowered by an unconventional bonding mechanism not observed in other prominent PV materials or isostructural oxide perovskites. This insight provides a blueprint for the design of tailored halide perovskites and related materials for PV applications.

Perovskites form a wide class of compounds where nearly all atoms of the periodic table can fit into their chemical formula ABX_3. The most studied perovskites were, for a long time, the oxides (X = O) due to their numerous applications including sonars (piezoelectric $PbZr_xTi_{1-x}O_3$—PZT),[15] photonics (electro-optic $LiNbO_3$),[16] capacitors (dielectric permittivity, $BaTiO_3$),[17] and infrared detectors (pyroelectric $LiTaO_3$, $PbTiO_3$).[18] Only very recently, a surge of interest has been stirred focusing on halide perovskites and their potential for optoelectronic devices, most notably at present for PV applications.[1–6]

To derive rational design rules for PV materials, it is helpful to understand the key microscopic parameters responsible for their properties. Several such properties have been identified, which determine the performance of PV materials (see also **Table 1**). To optimize their PV efficiency, materials should maximize their absorption in the visible range. They should also possess a high charge carrier mobility, which is facilitated by small effective masses. Both the optical absorption and the effective masses are governed by the nature of the valence and conduction band states involved. For the perovskites investigated here, these bands arise from the B—X bond in ABX_3 compounds, as also confirmed in the following section. In the following, we will study stoichiometric trends for the effective masses of electrons and holes as well as the optical absorption for halide and oxide perovskites. Since halide and oxide perovskites often show the same atomic arrangement but very different optoelectronic properties, this is indicative for important differences in the nature of the relevant electronic states. These dissimilarities will be related to a quantum-chemical bond analysis, which identifies and characterizes the orbitals and bonds responsible for the favorable PV properties. Subsequently, a map will be displayed based on the crucial bond parameters, which can be used to predict important trends in PV relevant properties. Finally, the insights obtained are used as input for a simple tight binding model that reproduces and explains all major findings.

Table 1. Desired material properties for the absorber material in a solar cell. Similar requirements can be listed for other optoelectronic devices such as photodiodes or solid state lasers.

Optical properties	Direct bandgap of 1.1–1.4 eV
	Sharp and steep absorption edge
	Low nonradiative recombination rate
Electrical properties	Charge carriers with high mobility μ
	Defect scattering small
Sample preparation	Ease of preparation of high-quality samples
	Low temperature preparation route
	Inexpensive and abundant elements

2. Favorable Material Properties Due to an Uncommon Bonding Mechanism

A crucial property for PV materials is the effective mass of the charge carriers in the vicinity of the Fermi level. These effective masses are inversely proportional to the curvature of the corresponding valence and conductance bands. Our calculations show striking differences for the oxide and halide perovskites as depicted in **Figure 1**. These results are robust against the choice of exchange correlation functional (strongly constrained and appropriately normed semilocal density functional (SCAN) or HSE06) including spin–orbit coupling. In the oxide perovskites, both the electron and the hole effective masses, i.e., m_e^* and m_h^*, are significantly larger than the free electron mass m_e. Such high effective masses are indicative of low mobilities, a major disadvantage for optoelectronic applications. The halide perovskites, on the contrary, have much lower effective masses. Both the electron and hole effective masses of the halide perovskites show a clear chemical trend. The replacement of I by Br and even more so Cl or F increases the corresponding electron and hole effective masses, in line with previous calculations for Sn-based halide perovskites.[19] To explain these trends, it is crucial to identify the orbital contributions to the different bands.

The dissimilarities between halide and oxide perovskites and the dependence of m_h^* on stoichiometry are indicative of systematic differences in the band structure in the vicinity of the Fermi energy, as depicted in **Figure 2**. Interestingly, the valence band (VB) structure reveals many similarities between the two perovskite families, while the conduction bands show more obvious differences. The main common feature of the valence bands is the location of the maximum at the *R*-point. This comes from the dominant role of the p-orbitals of the X atom in these bands, i.e., the O p-states for the oxide perovskites and the halogen p-states for the halide perovskites. Yet, there are two important differences comparing the valence bands of oxide and halide perovskites. The valence band maximum at the *R*-point for the halide perovskites also has a noticeable contribution from the Pb s-state, while the corresponding contribution from Ti is absent for the oxide perovskites. This Pb s-state has been stressed in previous studies, which attributed the favorable properties of halide perovskites to the role of the ns^2 configuration of the B cation, i.e., Pb $6s^2$ or Sn $5s^2$ ("lone-pair") states. Yet, there is a second important difference between the valence bands of halide and oxide perovskites. The dispersion of the valence band in the oxide perovskites is governed by the orbital overlap of oxygen p-states and transition metal (e.g., Ti, Zr, or Hf) d-states, while for the halide perovskites the valence band dispersion is strongly affected by the overlap of halogen p-states and metal (Sn or Pb) p-states. Since p-orbitals are responsible for the dispersion of the valence and conduction band in the halide perovskites, we observe a mirror-like symmetry of the conduction and valence bands. This finding helps us to understand why the effective masses of electrons and holes are similar in a given halide perovskite (see Figure 1).

Further differences are obvious for the conduction bands of oxide and halide perovskites. The conduction band minimum is located at different points in reciprocal space. This is due to the

© 2021 The Authors. Advanced Functional Materials published by Wiley-VCH GmbH

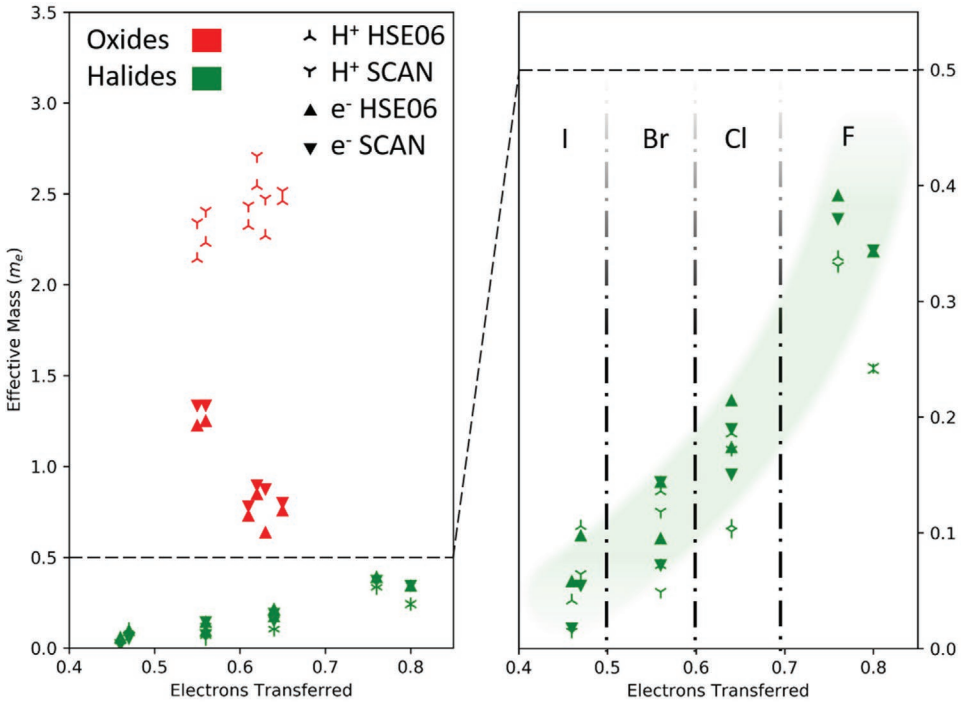

Figure 1. Effective masses of electrons and holes for oxide (red) and halide (green) perovskites. The effective masses for holes (three-pointed stars) and electrons (filled triangles) are computed with the SCAN (symbols pointing down) and HSE06 functional (symbols pointing up) including spin–orbit coupling. The effective masses of the halides are significantly smaller than those of the oxides. It is also noteworthy that for the halide perovskites the effective masses of the electrons and holes increase steadily with increasing relative electron transfer (ET) of the B atom to the surrounding X atoms (a quantity defined in more detail in the text). No such trend is found for the oxide perovskites.

different nature of the states in the conduction bands. For the halide perovskites the relevant states are predominantly p-states of the B atom, while for the oxide perovskites the d-states of the B atom (here, Ti) are important. Hence, it is unclear whether the contribution of lone-pair states or p–p interactions between adjacent B and X atoms (or both) is responsible for the favorably low effective masses in the halide perovskites. **Table 2** already provides data that question the hypothesis that s-states of the B-atom are responsible for the favorably low hole effective mass. Analyzing the different halide perovskites reveals that going from the iodine to bromine, chlorine, and finally fluorine halide perovskites leads to an increase of m_h*, even though the contribution of s-states of Pb (and Sn, respectively) to the density of states up to 5.5 eV below the Fermi energy E_F has increased. If these s-states would be the main factor governing the favorably low effective masses, one would expect a steady decrease of m* with increasing s-state contribution. This is not observed, questioning the hypothesis that the s-state contribution governs the favorably low effective mass of halide perovskites.

We will provide further arguments supporting the view that the s^2 state of the Sn or Pb atom is not the dominant factor explaining the favorable low effective mass of the halide perovskites after discussing the absorption of halide and oxide perovskites. As already stressed, the optical absorption is another crucial property of PV materials. They should have a bandgap between 1.1 and 1.4 eV, according to Shockley and Queisser.[20] This can be realized easily in the halide perovskites listed in Table S2 (Supporting Information). For oxide perovskites, $BaTiO_3$ has a larger bandgap of 3.2 eV, and the maximum absorption only occurs at 5.3 eV, too high for PV applications. Furthermore, the absorption should increase steeply above the bandgap. This is the case for both cubic oxide and halide perovskites, where $\varepsilon_2(\omega)$ i.e. epsilon imaginary reaches a pronounced maximum. Yet, there is a second difference between these two classes of perovskites. This can be seen upon decomposing the absorption to the contribution of transitions between different states; see **Figure 3**. For the oxides, the oxygen p–metal d-transition governs the absorption, while the oxygen s–metal d-transition hardly contributes. The halide perovskites, on the contrary, reveal a strong peak for I p- to Pb p-state transitions and a weak peak for the Pb s–Pb p contribution. This appears surprising at first sight, since often the selection rule from atomic physics is employed to explain absorption efficiencies, which demands a change of angular momentum by 1 for direct allowed transitions. Yet, in solids, it is the symmetry of the wavefunction (parity) for the initial and final states at the corresponding point in reciprocal state, which is decisive. At the important *R*-point, for example, "both" the Pb s–Pb p and I p–Pb p transitions are allowed (see also Figure 5). A quantitative decomposition reveals that 92% of the optical absorption below 4 eV come from p–p transitions, while s–p transitions are only responsible for 8% of the optical absorption. An increasing contribution of the cation (Sn or Pb) s-state to the upper valence band goes with an overall decrease of the optical absorption, as observed upon going from the iodine perovskites to the bromine and chlorine perovskites. This finding further questions the models in which Sn or Pb s-state governs the favorable PV

© 2021 The Authors. Advanced Functional Materials published by Wiley-VCH GmbH

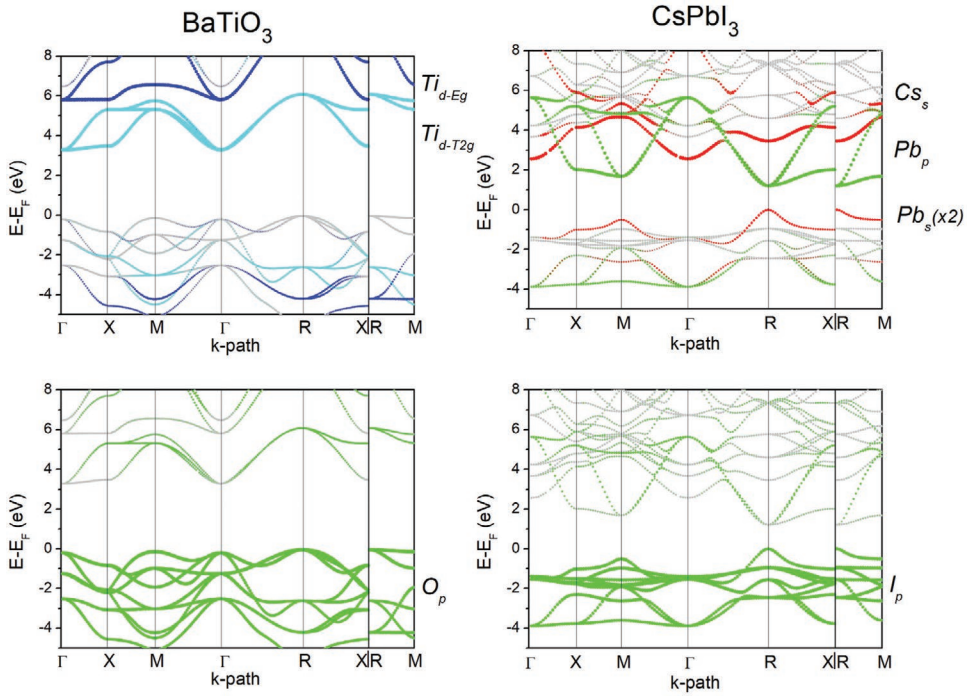

Figure 2. Band structure decomposition of two characteristic perovskites, $BaTiO_3$ (left) and $CsPbI_3$ (right). s-, p-, and d-states are plotted in red, green, and blue, respectively. The size of the symbols is proportional to the orbital contribution to the bands. Top panels: Fat bands (bands decomposed into the contributions of atomic orbitals) for Ti d_{xy}, d_{yz}, d_{xz} (cyan, labeled $Ti_{d\text{-}T2g}$), and Ti d_{x2-y2} and d_{3z2-r2} (blue, label $Ti_{d\text{-}Eg}$) in $BaTiO_3$ and Pb-p, Pb-s, and Cs-s in $CsPbI_3$. To improve the visibility of the Pb-s contribution, its magnitude has been increased by a factor of 2. The underlying band structure is plotted with gray symbols. Bottom panels: Fat bands for O-p in $BaTiO_3$ and I-p in $CsPbI_3$. The complete band structure is given in Figure S1 (Supporting Information). The calculations depicted here were performed with the SCAN functional without SOC.

material properties. We hence need to look elsewhere for an explanation of the trends seen in Table 2 and Figure 3.

3. Quantum-Chemical Analysis of Bonding in Halide Perovskites

To unravel the origin of the low effective masses of the halide perovskites and the strong optical absorption, we need to understand the relationship between the band structure and chemical bonding. To reach this goal, we employ quantum-chemical tools, in particular, the quantum theory of atoms in molecules (QTAIM).[21] With this theory, two quantities can be determined, which quantify differences in chemical bonding: the electron transfer (ET) and the number of electrons shared (ES) between pairs of neighboring atoms (see the "Experimental Section"[22–25]). To facilitate a comparison of different compounds, the relative ET is utilized, which is obtained upon dividing the total electron transfer by the oxidation state (nominal ionic charge). An electron sharing between neighboring atoms equal to two corresponds to the Lewis picture of a perfect covalent bond, i.e., an equally shared electron pair. ET and ES are accurate quantum-chemical bond indicators, which can separate the different types of bonding, as shown in **Figure 4**. Materials that employ ionic bonding are located in the lower right corner of the map, since they are characterized by significant relative electron transfer. In covalent compounds, on the contrary, up to two electrons (an electron pair) are shared between single-bonded neighboring atoms (upper left corner). We can now explore how the bonding in perovskites compares with metallic, ionic, and covalent bonding, and hence where the bonds in the different perovskites are located on the map.

The majority of the compounds depicted in the map are either elements or binary compounds of A–B type, where a single type of bond is sufficient to brand the solid. In ABX_3 perovskites, on the contrary, we have to describe the A—X and B—X bonds separately, since they will be characterized by different values for the number of electrons shared and transferred.

Table 2. For halide perovskites, m^* (h, e), bandgap value, optical dielectric constant ε_∞, height of the absorption maximum versus fraction of s-states in the upper valence density of states (DOS) (E_F = 5.5 eV to E_F) and percentage of s-state at the valence band maximum. Effective masses and bandgap energies are computed with HSE06 and SOC. Other quantities are obtained using the SCAN functional.

Halide perovskite	s % DOS	s % VBM	m_h^*	m_e^*	E_g [eV]	ε_∞	Max abs.
$CsSnF_3$	33%	49%	0.241	0.343	1.99	3.45	3.40
$CsSnCl_3$	48%	65%	0.106	0.174	1.00	4.68	3.53
$CsSnBr_3$	35%	51%	0.072	0.095	0.49	6.23	4.06
$CsSnI_3$	29%	42%	0.042	0.058	0.28	8.59	7.26
CsPbF3	20%	31%	0.338	0.391	2.94	2.88	2.87
$CsPbCl_3$	22%	26%	0.186	0.214	1.71	3.10	2.98
$CsPbBr_3$	16%	20%	0.136	0.143	1.13	4.38	4.28
$CsPbI_3$	12%	14%	0.105	0.097	0.76	5.56	7.59

© 2021 The Authors. Advanced Functional Materials published by Wiley-VCH GmbH

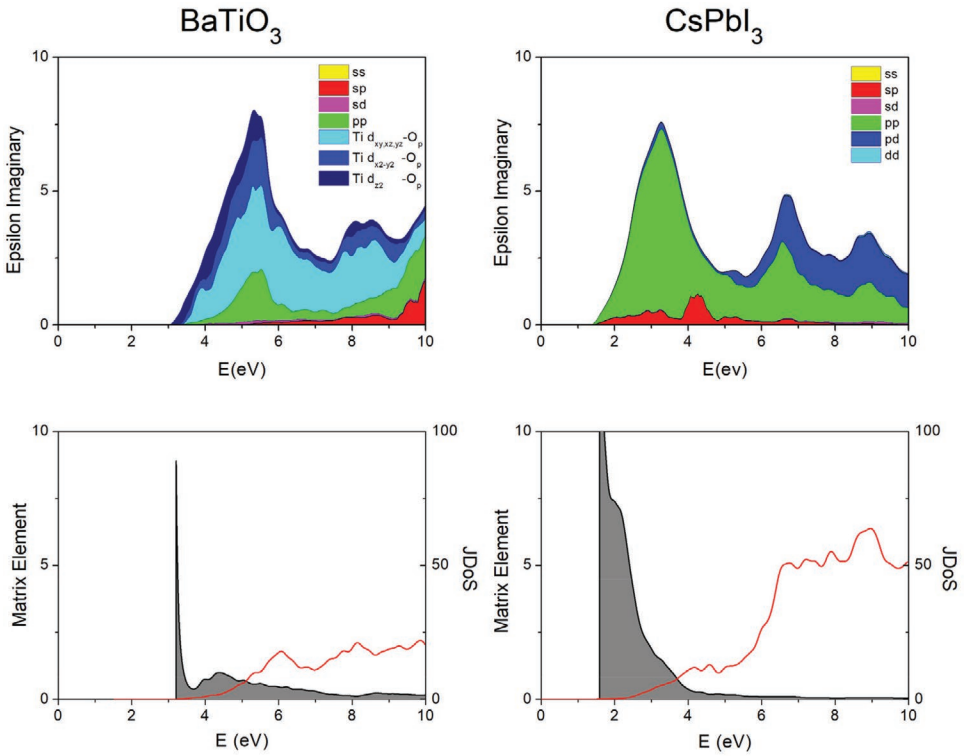

Figure 3. Absorption (epsilon imaginary) for $BaTiO_3$ and $CsPbI_3$ (top), decomposed into the joint density of states (red) and the corresponding average matrix element (shaded area, bottom). In $CsPbI_3$, the absorption maximum is observed at lower energy. It benefits from a large matrix element, dominated by p–p transitions. The optical properties of halide perovskites are thus far superior for PV applications. The joint density of states (JDoS) is in 1 eV^{-1}; the effective matrix element (eV) is defined here as the dielectric constant divided by the JDoS. Data obtained with the SCAN functional (see also Figure 5).

This enables us to relate different properties (see Table S1 in the Supporting Information) to these two different bonds and will help us to unravel the structure–property relationship based on an in-depth understanding of chemical bonding. In the following, we will focus first on undistorted perovskites, i.e., perfectly cubic systems with $Pm\bar{3}m$ symmetry. By comparing halide- and oxide-based perovskites that share the same crystal structure, we can also explore which material properties are governed by differences in bonding. The resulting data are summarized in Figure 4.

Figure 4 reveals that the A—X bond is always ionic, both for the oxide and the halide perovskites. On the contrary, the B—X bonds differ between the two perovskite families. The assignment of a bond as being ionic or covalent is accomplished based on the corresponding material properties.[26] To distinguish between ionic and covalent bonds, the coordination number and the chemical bond polarizability are employed. In Table S1 (Supporting Information), it is shown that the A—X bonds in oxide and halide perovskites closely resemble each other and are identified as ionic bonds. The B—O bond in the oxides, on the contrary, is best described as iono-covalent. There are both considerable charge transfer and significant sharing of electrons, i.e., a combination of significant ionic and covalent bonding contributions. Here, we focus on the B—X bond, which is responsible for the PV properties of the halide perovskites as we have shown (Figures 1–3). Interestingly, as shown in Figure 4, the B—X bond in the halide perovskites is located in a distinct, neighboring region, next to the iono-covalently bonded compounds. While there is significant electron transfer, ET is considerably smaller for the B—X than the A—X bond. Yet, it is also not a typical iono-covalent bond either, since the corresponding ES values are clearly below those of the B—O bonds. Furthermore, for a covalent bond involving halogen atoms, one expects an effective coordination number of 1 for the halogens, as observed in fluorocarbons, for example. The coordination number of 2 for the halogen atoms in halide perovskites leads to highly electronic charge deprived A—X bonds, formally to 2c—1e bonds, hence, incompatible with standard 2c—2e covalent bonds. Indeed, the ES values for the A—X bonds resemble those found in metavalently bonded compounds such as PbTe or PbSe.[28] This is no coincidence but instead indicative of a common type of bonding invoked in both halide perovskites and lead chalcogenides as will be discussed in the following sections.

The domain-averaged Fermi holes' (DAFH) analysis (Section SIII, Supporting Information) provides further precious insights into the relationship between metavalent bonding and favorable properties in the halide perovskites. The DAFH approach provides an ideal bridge between QTAIM and orbital-based descriptors. It is increasingly being used to characterize chemical bonding in systems with conventional and nonconventional bonding patterns in terms of (rigorously defined) localized functions resembling localized orbitals. Their occupation numbers and shape are derived through the Fermi hole function averaged over properly chosen domains, which, in our case, have been taken as the QTAIM basins that we adopted for

© 2021 The Authors. Advanced Functional Materials published by Wiley-VCH GmbH

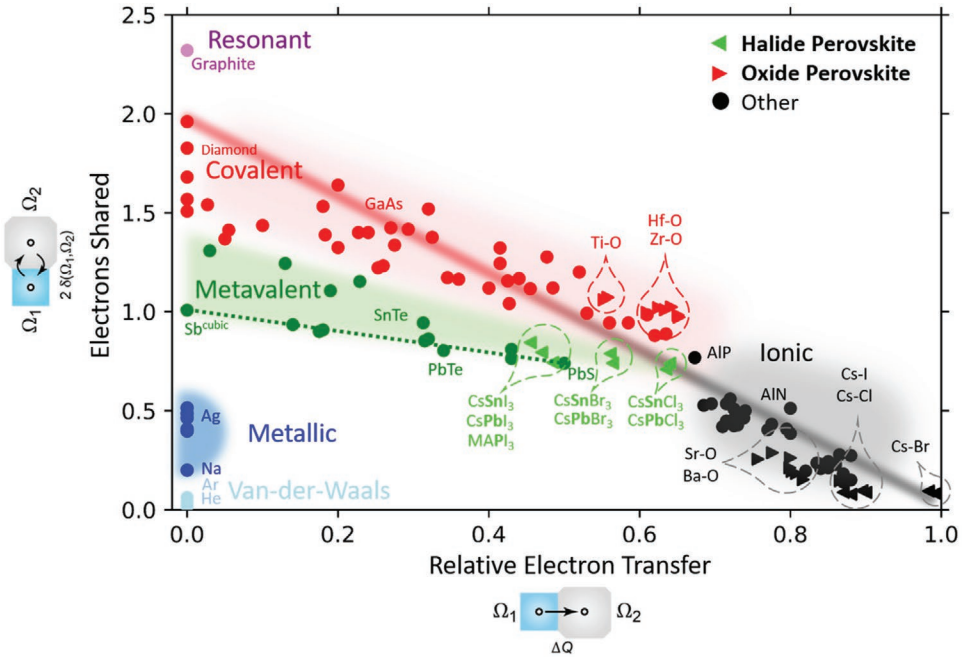

Figure 4. a) 2D map describing the bonding in solids. The map is spanned by the number of electrons shared between adjacent atoms and the electron transfer renormalized by the oxidation state. Different colors characterize different material properties[26] and have been related to different types of bonds.[27] Triangles pointing left are utilized for halide perovskites, and those pointing right for oxide perovskites. For these compounds, the element in bold characterizes the bond considered. Interestingly, the bonds for the different perovskites in this figure fall into three distinctively different classes. The A atom in the ABX_3 perovskites employs an ionic bond to its neighbors in both oxide and halide perovskites. The B—X bond instead differs in oxide and halide perovskites. While the B—X bond in oxide perovskites can be best described as iono-covalent, the B—X bond in halide perovskites shows the characteristic features of metavalent bonds. It is also noteworthy that the B—X bond in the halide perovskites is found in close vicinity of several lead chalcogenides, which show similar properties. The red–black line describes the transition from ideal covalent bonds to perfect ionic bonds. The dashed green line indicates metavalently bonded solids with perfect octahedral arrangement. MAPI stands for $CH_3NH_3PbI_3$.

the ES and ET evaluation. DAFH analysis (Section SIII, Supporting Information) reveals that the predominant contribution to the number of electrons shared in the B—X bond (B = Pb) comes from the overlap of the p—σ DAFH orbitals of B and X atomic domains, while the contribution from the s-like DAFH orbital of B or the lone-pair p DAFH orbitals of X is about four to six times lower. This is due to the fact that both these latter DAFH orbitals, at variance with the p—σ DAFH ones, mostly reside on the individual B or X atoms and are hardly shared between the two atoms (see Tables S3–S6 in the Supporting Information). The difference in bonding aptitude between the two sets of orbitals is even more impressive when considering that the population of the s-like DAFH orbital of B or of the lone-pair p DAFH orbitals of X is (much) larger. Thus, DAFH analysis clearly demonstrates that the dominance of the p–p transitions and the minor role played by the s–p transitions in the optical absorption below 4 eV are intimately related to the occurrence of the B—X metavalent bond and not to the s-like or p-like lone pairs on B and X, respectively.

As depicted in **Figure 5**, on the left-hand side (and in Table S3 in the Supporting Information), both for Pb and I atoms, the outermost atomic orbitals are p-orbitals. In the solid (center of Figure 5), their overlap is shown, leading to the formation of a σ-bond. The actual number of shared electron pairs is determined by the quantum-chemical calculations (Table S3, Supporting Information). Between adjacent Pb and I atoms a σ-bond is formed, which contains 0.8 electrons shared between the two atoms (see Figure 4), in line with a standard analysis of the density-functional theory (DFT) data (Table S8, Supporting Information), while for an ordinary covalent bond we would expect two electrons being shared between adjacent atoms. Slightly lower values are obtained for the Pb—Br bond in $CsPbBr_3$ and the Pb—Cl bond in $CsPbCl_3$. Hence, with about one electron (a half-filled orbital) between adjacent Pb and I atoms and significant overlap of the outermost atomic orbitals, we are expecting a metallic band, as shown on the right-hand side of Figure 5. Halide perovskites are, hence, incipient metals,[26] i.e., have an almost metallic ground state. Such incipient metals have a number of characteristic features including a high Born effective charge, a measure of the high polarizability of the B—X bond, an effective coordination number incompatible with the 8-*N* rule for ordinary covalent bonding, a soft crystalline lattice, and high values of the optical dielectric constant. All of the properties are also found for halide perovskites. Some of the properties are directly related to the favorable PV properties of halide perovskite.[29–31] The combination of a high optical dielectric constant and large Born effective charges ensures, for example, that the state dielectric constant is even considerably higher.[32,33] This ensures that carrier scattering is reduced.[34]

More importantly, the metavalent character of the B—X bond also explains why halide perovskites are such good absorbers and possess charge carriers (both holes and electrons) with small effective masses as explained in more detail in the following sections. Before discussing how the insights obtained

© 2021 The Authors. Advanced Functional Materials published by Wiley-VCH GmbH

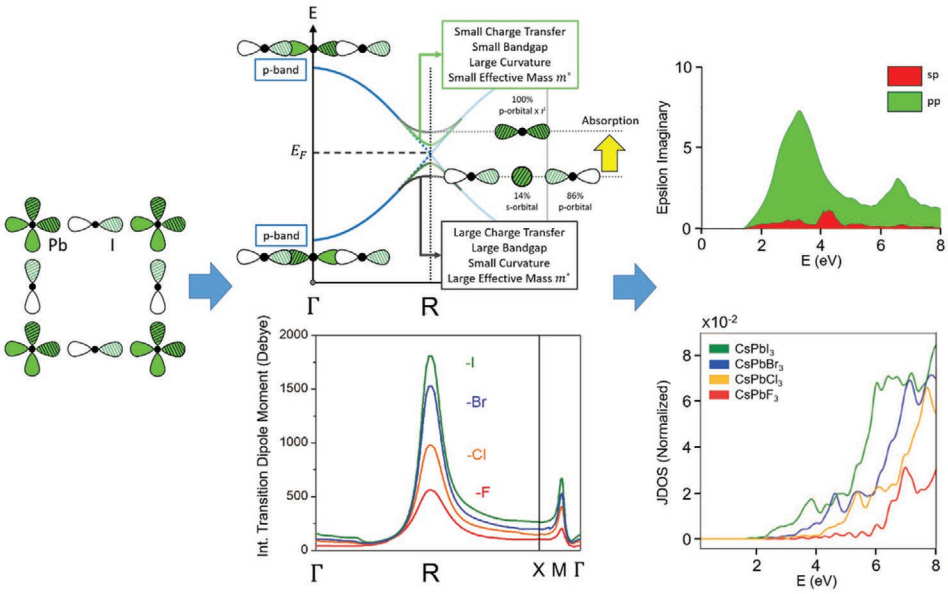

Figure 5. Bond formation and resulting band structure as well as optical properties in $CsPbI_3$. Atomic p-orbitals of Pb and I responsible for bond formation are depicted on the left-hand side (1D representation). The atomic arrangement is characterized by small electron transfer and the formation of σ-bonds between adjacent atoms. These σ-bonds are occupied by about half an electron pair (ES ≈ 1), resulting in a metallic band (dashed blue band). However, the electron transfer creates a bandgap at *R* (green/grey band). At Γ, the p-σ states are perfectly bonding (valence band) or antibonding (conduction band), and involve equally the Pb-p and I-p orbitals (left panel). At the *R* point, the top of the valence consists of 86% I-p and only 14% Pb-s (right panel). The symmetry is such that all interactions are (weakly) bonded. Upon absorption, the transition occurs at the bottom of the conduction band, that is 100% Pb-p. The parity of this orbital is odd, but the product with the dipolar operator makes the state fully symmetric. Therefore, the absorption transition is allowed to this state from both Pb-s and I-p components of the valence band. The relative contribution of these orbitals to the valence band at the *R*-point, and the larger overlap between neighboring p orbitals is responsible for the much larger p–p absorption. This contribution at the *R*-point shows a clear chemical trend, i.e., it goes down from iodine to bromine, chlorine, and fluorine perovskite. This decrease is attributed to a smaller overlap of the halogen and Pb p-states, while the joint density of states has the same form and maxima for all four lead perovskites and is only shifted in energy.

can be utilized to tailor materials for PV applications, we discuss in the Supporting Information how the transition from inorganic halide perovskites to hybrid organic–inorganic halide perovskites will alter PV material properties. Both the impact of an organic molecule at the A-site and distortions of the B atom away from a perfect octahedral arrangement can be described in the framework presented here. It should be noted that possible structural distortions have to remain moderate to preserve metavalence.[27] Indeed, several studies of chalcogenide phase change materials pointed to the fact that σ-bonds of p-orbitals can evolve toward covalence with the appearance of disorder, accounting for the electrical and optical contrasts.[35,36]

4. A Simple Tight Binding Model to Explain and Predict Property Trends

Based on the quantum-chemical bond analysis, we can build a simple tight binding model (Section SIV, Supporting Information) focusing on the σ-bonds formed by p-orbitals of adjacent B and X atoms. A similar model had already been put forward by Goesten and Hoffmann,[37] who noticed a mirror symmetry between the top of the valence and the bottom of the conduction band, which is best explained if the importance of I p in the valence band is similar to that of Pb p in the conduction band. Hence, we consider a chain of I p- and Pb p-orbitals with distance a and onsite energies (ε_{Ip}, ε_{Pbp}), as well as resonance integral β_{pp} between them, setting $\varepsilon_{I-p} - \varepsilon_{Pb-p} = 2\Delta$. In this case, one obtains $E_G = 2\Delta$, while the effective mass at *R* equals $\pm\frac{1}{\hbar^2}\frac{\Delta}{a^2\beta^2}$. A decrease of charge transfer, i.e., smaller Δ and thus smaller E_G, hence leads to smaller effective masses. For vanishing charge transfer and perfect octahedral alignment, the system would even be a metal. Yet, there are two mechanisms, which will open a bandgap, a necessity for PV materials. These are either distortions of the linear alignment for the B—X—B chain (Peierls distortions) and/or charge transfer. This opening of the bandgap has also a strong impact on the charge carriers. The sketch in Figure 5 already reveals that an increasing bandgap leads to a larger effective mass, in line with the data (see Figure 1). The simple tight binding model confirms these claims. The nature of the B—X bonds is, hence, responsible for the favorably small effective masses of the halide perovskites. The pronounced overlap of the halogen p-orbital and the p-orbital of the B-atom (Pb or Sn) also explains the pronounced optical absorption as schematically depicted in Figure 5. Indeed, Figure 5 shows that for $CsPbI_3$ the predominant contribution to the optical absorption is due to the p–p transition. It is this unconventional electronic structure, which characterizes halide perovskites as third-generation PV materials.[11]

Figure 5 reveals that both the small effective mass of the charge carriers and the pronounced optical absorption are

© 2021 The Authors. Advanced Functional Materials published by Wiley-VCH GmbH

explained by the unconventional bonding mechanism in halide perovskites. This is a striking difference to tetrahedral semiconductors such as Si, Ge, or GaAs. In these covalent solids, a decrease of the effective mass of the charge carriers is not accompanied by a concomitant increase of the optical absorption. This sheds further light on the favorable PV properties of halide perovskites.

5. Conclusions and Outlook

As we have shown, the bonding configuration in halide perovskites is distinctively different from metallic, ionic, and covalent bonding. The bonding mechanism and the model explaining their optical properties are also valid in the case of the actual hybrid perovskite, where the limited angular and linear distortions preserve the essential bonding features. This unconventional bonding is responsible for many of their favorable PV characteristics. One should thus expect similarly attractive properties in other materials, which employ this type of bonding. As shown in Section SIX (Supporting Information), the band structures of lead chalcogenides closely resemble those of halide perovskites. In both cases, the p-states in the vicinity of the Fermi level form half-filled σ-bonds, leading to small effective masses and a strong optical absorption. Interestingly, the optical absorption is even significantly higher for lead chalcogenides since the chalcogen and lead atoms form six σ-bonds each, while a halogen atom only forms two σ-bonds in the perovskites. One can hence hope to realize significantly stronger optical absorption and favorable PV properties in other chalcogenides and related compounds, if materials are identified, which have a sufficient bandgap. What is crucial though is to realize bonding configurations with half-filled σ-bonds of p-orbitals with sufficient overlap.[38]

The comparison of halide perovskites and lead telluride also helps in understanding another important aspect, i.e., charge transport. For both material classes, transport is governed by the overlap of the p-orbitals of the adjacent atoms. This overlap depends upon ET, the charge transfer between both atoms and the degree of distortion away from a perfect octahedral arrangement, which leads to increasing ES values. Hence, ET and ES can be considered as the natural variables to describe many relevant properties such as m^*, the strength of the optical absorption, Z^*. For charge transport, the effective masses play a prominent role. Yet, other properties are also important. Halide perovskites form soft and rather anharmonic lattices, which, in principle, lead to electron–phonon coupling.

Deviations away from the perfect octahedral arrangement, even if only dynamic, i.e., upon excitation of an optical phonon, lift the degeneracy of the p-states and the inversion symmetry.[39] Lifting of the inversion symmetry leads to ferroelectric behavior. It is also one of the conditions to observe the Rashba effect. Therefore, many chalcogenides with octahedral-like atomic arrangement show this effect if they exhibit a distortion that destroys inversion symmetry. Chalcogenides that exhibit metavalent bonding (MVB) possess a propensity for such distortions, i.e., Peierls distortions. This is well known for GeTe. SnTe is more interesting. It shows a cubic structure (inversion symmetry and no Peierls distortion) at room temperature. Yet, in very thin films it exhibits a Peierls distortion[40] and hence also shows a Rashba splitting. Such a Rashba splitting is also shown in bulk SnTe at low temperatures, which stabilize a ferroelectric distortion.[41] Interestingly, in thin films, MVB can help us to understand why a Peierls distortion forms in SnTe. In thin films, the competition between electron delocalization and electron localization changes. For thin films, electron localization and hence increasing Peierls distortions are observed leading to a concomitant increase of ES[42] and thus also a strong Rashba effect. The second condition to observe the Rashba effect is strong spin–orbit coupling. Spin– orbit coupling scales with the nuclear charge. Hence, heavy atoms are favorable to detect this effect. For atoms in this region of the periodic table, which, in addition, are governed by the overlap of adjacent p-orbitals, the Rashba effect is frequently observed. Hence, metavalent bonding, ferroelectric behavior, and the Rashba effect are closely interwoven. One could say that the unique bonding enables these effects.

Metavalent bonding has another favorable consequence. It leads to a high value of ε_{static},[43] which ensures that screening of charged defects is very efficient. This reduces defect scattering and has a favorable impact on the lifetime of the charge carriers. It also reduces the coupling between electronic motion and lattice distortions and the concomitant mass renormalization, which scales with $(1/\varepsilon_{static} - 1/\varepsilon_{\infty})$. Therefore, the carrier's lifetime is longer,[44] which ensures a high-mobility life-time product, a key factor for the efficiency of these PV materials.[11,45,46]

The quantum-mechanical indicators computed also allow us to extract important trends that can help designing future PV materials. The two most important chemical bond descriptors for halide perovskites are the number of electrons shared and transferred for the B−X bond. Both impact the optical absorption. Increasing the number of electrons shared between adjacent atoms increases the Peierls distortion and hence reduces the orbital overlap. This immediately decreases the optical absorption and increases the bandgap.[47] Similarly, an increasing electron transfer also reduces the optical absorption and increases the bandgap, as shown recently for the related lead chalcogenides.[48] Hence both ET and ES can be employed to tailor the optical absorption and the bandgap. **Figure 6** shows, for instance, how the bandgap varies with the number of shared and transferred electrons. Among all compounds for which the data have been computed, the halide perovskites occupy a well-defined area of the metavalent region of the map.

The compounds that we have computed are characterized by an octahedral arrangement of the B atom. These halide perovskites are all located in the vicinity of the dashed line in Figure 4, where we also find the octahedrally coordinated lead chalcogenides. As can be seen from a comparison of $CsSnI_3$, $CsSnBr_3$, and $CsSnCl_3$, their bandgap is largely controlled by the electron transfer. Increasing the electron transfer, or alternatively the number of electrons shared, while maintaining metavalent bonding increases the bandgap, yet preserves reasonably small effective masses and strong optical absorption. The numbers of electrons shared and transferred between adjacent atoms are thus bonding descriptors, which enable the design of a map that separates different bonding mechanism in solids. Yet, ES and ET are also property predictors since they control

© 2021 The Authors. Advanced Functional Materials published by Wiley-VCH GmbH

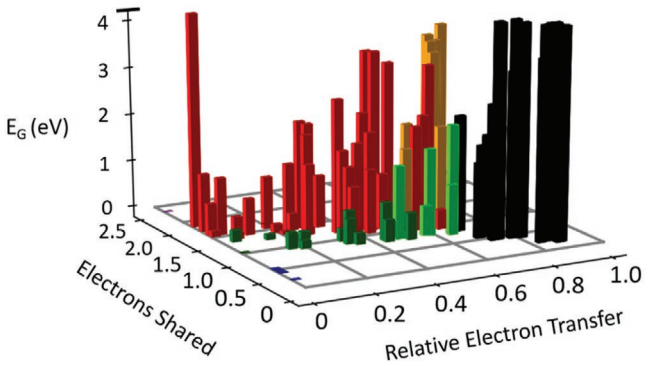

Figure 6. Bandgap as a function of electrons transferred and shared. Different types of bonds are denoted by different colors, i.e., ionic (black), covalent (red), metallic (blue), metavalent (green), halide perovskites (light green), and oxide perovskites (orange). Metavalently bonded systems like PbTe or $CsSnI_3$ are characterized by sharing about one electron between adjacent atoms and modest charge transfer, leading to small bandgaps, strong optical absorption, and small effective masses. The number of electrons shared and transferred can be employed to tune the bandgap and related PV properties.

the crucial optoelectronic properties of halide perovskites like the effective mass of the charge carriers at the Fermi level and the optical absorption. Another option to fine-tune the optical properties is to tailor the interatomic distance. Both for gaps created by charge transfer (halide perovskites and lead chalcogenides) and gaps created by Peierls distortions, expanding the metavalent σ–bond increases the gap. Therefore, one can, e.g., modify the A atom in ABX_3 halide perovskites to stretch the B—X bond or use strain engineering. The map in Figure 4, hence, could be used as a blueprint to design third-generation PV materials.

6. Experimental Section

All structure and electronic structure calculations were performed using density functional theory in combination with projector augmented wave (PAW)[49] potentials, as implemented in the ABINIT[50,51] and VASP (Vienna ab initio simulation *package*) codes.[52–56] Different exchange-correlation functionals were used. The SCAN meta-generalized gradient approximation (GGA) functional[57] was used together with the VASP code to compute ground state electronic properties. This functional was shown to outperform common local functionals.[58] In particular, it yielded gap values that were closer to the experimental ones, although these remained underestimated. It was also shown to be superior to hybrid functionals to reproduce the dynamics and structural distortions in hybrid perovskites.[59]

Density functional perturbation theory[60–62] was used to compute the dielectric properties (dielectric constant and Born effective charges). In one case ($BaTiO_3$), the scissors correction was computed employing the HSEO6 hybrid functional.[63] The structures were relaxed with 550 eV plane-wave energy cutoff until residual forces were less than 10^{-5} eV $Å^{-1}$. The *k*-point grids were $8 \times 8 \times 8$ (hybrid functional) to $16 \times 16 \times 16$ (non-hybrid functional) for oxide and halide perovskites, and $4 \times 2 \times 4$ for the hybrid methylammonium-lead-iodide (MAPI) ($CH_3NH_3PbI_3$). Spin–orbit corrections were included in selected calculations (effective masses and gap). The inclusion of spin–orbit coupling (SOC) on the MAPI hybrid perovskites was also tested, reaching the conclusion that SCAN + SOC lowers the effective masses, particularly for the electrons, when compared to SCAN without SOC (m_h^* = (0.18; 0.12; 0.18) vs (0.24; 0.15; 0.24) and m_e^* = (0.14; 0.08; 0.14) vs (1.00; 0.06; 0.93)).

To compute the electrons shared and transferred, Bader basins Ω[64] were defined using the Yu–Trinkle algorithm[65] and the corresponding localization (LI(Ω)) and delocalization indices (δ (Ω_1, Ω_2))[66] were determined using the DGRID code.[67] The initial wavefunctions were computed with ABINIT and the Perdew–Burke-Ernzerhof-GGA exchange correlation.[68] The LIs were obtained by double integration of the same spin part of exchange-correlation hole over the corresponding basin, while delocalization indexes (DIs) were obtained by integration of the same quantity once over the native basin and once over another basin. LI shows how many electron pairs are localized within the basin and do not participate in bonding, while DI provides the number of shared pairs of electrons between two atoms. The sum over the localization and half of the delocalization indices of an atom with all other basins equals, within numerical errors, the electron population of each atom $N(\Omega)$. The same is much more simply obtained by integration of the electron density over the basin Ω. The total number of electrons transferred, TET, from an electropositive atom Ω to its bonded atoms is obtained by subtracting from its nuclear charge, $Z(\Omega)$, its electron population $N(\Omega)$, $TET(\Omega) = Z(\Omega) - N(\Omega)$. For the ABX_3 perovskites investigated in this study, the electron transfer from an A or B atom to one of their bonded X atoms was, respectively, given by TET(A)/*n* or TET(B)/*m*, with *n* and *m* being the total number of their bonded X atoms. The relative values of such A(B) → X electron transfers were then obtained by dividing the electron transfers by the negative of the formal oxidation charge of X (1 for halogen and 2 for O atoms). The values obtained for ET and ES were barely affected by the choice of the functional. This is no surprise, since these quantities depend mostly on the valence wavefunction.

Supporting Information

Supporting Information is available from the Wiley Online Library or from the author.

Acknowledgements

The authors acknowledge the computational resources granted from RWTH Aachen University under project RWTH0508, as well as JARA0183 and JARA0198 in the initial project stage, kindly provided by Riccardo Mazzarello. This work was supported in part by the Deutsche Forschungsgemeinschaft (SFB 917), in part by the Federal Ministry of Education and Research (BMBF, Germany) in the project NEUROTEC (16ES1133 K), and in part by Excellence Initiative of the German Federal and State Governments (EXS-SF-neuroIC005). E.B. and J.-Y.R. acknowledge support from FNRS and computational resources provided by the CÉCI (funded by the F.R.S.–FNRS under Grant No. 2.5020.11) and the Tier-1 Supercomputer of the Fédération Wallonie-Bruxelles (infrastructure funded by the Walloon Region under Grant Agreement No. 1117545). E.B. acknowledges the FNRS CDR project MULAN (J.0020.20). J.-Y.R. acknowledges the FNRS CDR project ABIGLO (J.0154.21).

Open access funding enabled and organized by Projekt DEAL.

Conflict of Interest

The authors declare no conflict of interest.

Author Contributions

J.R. suggested a metavalent bonding mechanism in halide perovskites. M.W. initiated and conceptualized the project. J.-Y.R. and C.-F.S. performed the tight-binding and DFT calculations, with early contributions from M.S. E.B. performed DFT calculations and provided insights into oxide perovskites, while P.G. helped with the DAFH

© 2021 The Authors. Advanced Functional Materials published by Wiley-VCH GmbH

analysis. The paper was written by M.W. with contributions from J.-Y.R. and C.-F.S., and support from all co-authors. All authors have given approval to the final version of the manuscript.

Data Availability Statement

The data that support the findings of this study are available from the corresponding author upon reasonable request.

Keywords

effective mass, halide perovskites, metavalent bonding, optical absorption, photovoltaics

Received: October 8, 2021
Published online: October 23, 2021

[1] A. Kojima, K. Teshima, Y. Shirai, T. Miyasaka, *J. Am. Chem. Soc.* **2009**, *131*, 6050.
[2] H.-S. Kim, C. R. Lee, J. H. Im, K. B. Lee, T. Moehl, A. Marchioro, S. J. Moon, R. Humphry-Baker, J. H. Yum, J. E. Moser, M. Gratzel, N. G. Park, *Sci. Rep.* **2012**, *2*, 591.
[3] M. Liu, M. B. Johnston, H. J. Snaith, *Nature* **2013**, *501*, 395.
[4] M. A. Green, A. Ho-Baillie, H. J. Snaith, *Nat. Photonics* **2014**, *8*, 506.
[5] M. Kulbak, D. Cahen, G. Hodes, *J. Phys. Chem. Lett.* **2015**, *6*, 2452.
[6] H. J. Snaith, *Nat. Mater.* **2018**, *17*, 372.
[7] D. B. Mitzi, K. Chondroudis, C. R. Kagan, *IBM J. Res. Dev.* **2001**, *45*, 29.
[8] D. B. Mitzi, S. Wang, C. A. Feild, C. A. Chess, A. M. Guloy, *Science* **1995**, *267*, 1473.
[9] L. N. Quan, F. P. García de Arquer, R. P. Sabatini, E. H. Sargent, *Adv. Mater.* **2018**, *30*, 1801996.
[10] D. A. Egger, A. Bera, D. Cahen, G. Hodes, T. Kirchartz, L. Kronik, R. Lovrincic, A. M. Rappe, D. R. Reichman, O. Yaffe, *Adv. Mater.* **2018**, *30*, 1800691.
[11] W. J. Yin, J. H. Yang, J. Kang, Y. F. Yan, S. H. Wei, *J. Mater. Chem. A* **2015**, *3*, 8926.
[12] J. M. Frost, K. T. Butler, F. Brivio, C. H. Hendon, M. van Schilfga arde, A. Walsh, *Nano Lett.* **2014**, *14*, 2584.
[13] T. M. Brenner, D. A. Egger, L. Kronik, G. Hodes, D. Cahen, *Nat. Rev. Mater.* **2016**, *1*, 15007.
[14] D. H. Fabini, R. Seshadri, M. G. Kanatzidis, *MRS Bull.* **2020**, *45*, 467.
[15] K. Uchino, *Sci. Technol. Adv. Mater.* **2015**, *16*, 046001.
[16] N. Courjal, M.-P. Bernal, A. Caspar, G. Ulliac, F. Bassignot, L. Gauthier-Manuel, M. Suarez, *Lithium Niobate Optical Waveguides and Microwaveguides*, IntechOpen Limited, London, UK **2018**.
[17] J. F. Scott, *Science* **2007**, *315*, 954.
[18] S. P. Alpay, J. Mantese, S. Trolier-McKinstry, Q. Zhang, R. W. Whatmore, *MRS Bull.* **2014**, *39*, 1099.
[19] L. Y. Huang, W. R. L. Lambrecht, *Phys. Rev. B* **2013**, *88*, 12.
[20] W. Shockley, H. J. Queisser, *J. Appl. Phys.* **1961**, *32*, 510.
[21] R. F. W. Bader, *Acc. Chem. Res.* **1985**, *18*, 9.
[22] M. Rahm, *J. Chem. Theory Comput.* **2015**, *11*, 3617.
[23] A. I. Baranov, M. Kohout, *J. Comput. Chem.* **2011**, *32*, 2064.
[24] P. Golub, A. I. Baranov, *J. Chem. Phys.* **2016**, *145*, 154107.
[25] A. Otero-de-la-Roza, E. R. Johnson, V. Luaña, *Comput. Phys. Commun.* **2014**, *185*, 1007.
[26] M. Wuttig, V. L. Deringer, X. Gonze, C. Bichara, J.-Y. Raty, *Adv. Mater.* **2018**, *30*, 1803777.
[27] J. Y. Raty, M. Schumacher, P. Golub, V. L. Deringer, C. Gatti, M. Wuttig, *Adv. Mater.* **2019**, *31*, 1806280.
[28] S. Maier, S. Steinberg, Y. Cheng, C.-F. Schön, M. Schumacher, R. Mazzarello, P. Golub, R. Nelson, O. Cojocaru-Mirédin, J.-Y. Raty, M. Wuttig, *Adv. Mater.* **2020**, *32*, 2005533.
[29] A. K. U. Michel, A. Hessler, S. Meyer, J. Pries, Y. Yu, T. Kalix, M. Lewin, J. Hanss, A. De Rose, T. W. W. Mass, M. Wuttig, D. N. Chigrin, T. Taubner, *Adv. Mater.* **2019**, *31*, 1901033.
[30] A. C. Ferreira, S. Paofai, A. Letoublon, J. Ollivier, S. Raymond, B. Hehlen, B. Ruffle, S. Cordier, C. Katan, J. Even, P. Bourges, *Commun. Phys.* **2020**, *3*, 48.
[31] T. Lanigan-Atkins, X. He, M. J. Krogstad, D. M. Pajerowski, D. L. Abernathy, N. M. N. X. Guangyong, Z. Xu, D.-Y. Chung, M. G. Kanatzidis, S. Rosenkranz, R. Osborn, O. Delaire, *Nat. Mater.* **2021**, *20*, 977.
[32] C. Chen, P. Jost, H. Volker, M. Kaminski, M. Wirtssohn, U. Engelmann, K. Kruger, F. Schlich, C. Schlockermann, R. Lobo, M. Wuttig, *Phys. Rev. B* **2017**, *95*, 094111.
[33] P. Ghosez, J. P. Michenaud, X. Gonze, *Phys. Rev. B* **1998**, *58*, 6224.
[34] W. M. Ming, H. L. Shi, M. H. Du, *J. Mater. Chem. A* **2016**, *4*, 13852.
[35] K. Shportko, S. Kremers, M. Woda, D. Lencer, J. Robertson, M. Wuttig, *Nat. Mater.* **2008**, *7*, 653.
[36] B. Huang, J. Robertson, *Phys. Rev. B* **2010**, *81*, 4.
[37] M. G. Goesten, R. Hoffmann, *J. Am. Chem. Soc.* **2018**, *140*, 12996.
[38] W. Welnic, S. Botti, L. Reining, M. Wuttig, *Phys. Rev. Lett.* **2007**, *98*, 236403.
[39] Z. Liu, C. Vaswani, X. Yang, X. Zhao, Y. Yao, Z. Song, D. Cheng, Y. Shi, L. Luo, D. H. Mudiyanselage, C. Huang, J. M. Park, R. H. J. Kim, J. Zhao, Y. Yan, K. M. Ho, J. Wang, *Phys. Rev. Lett.* **2020**, *124*, 157401.
[40] K. Chang, J. W. Liu, H. C. Lin, N. Wang, K. Zhao, A. M. Zhang, F. Jin, Y. Zhong, X. P. Hu, W. H. Duan, Q. M. Zhang, L. Fu, Q. K. Xue, X. Chen, S. H. Ji, *Science* **2016**, *353*, 274.
[41] E. Plekhanov, P. Barone, D. Di Sante, S. Picozzi, *Phys. Rev. B* **2014**, *90*, 161108.
[42] I. Ronneberger, Z. Zanolli, M. Wuttig, R. Mazzarello, *Adv. Mater.* **2020**, *32*, 2001033.
[43] B. J. Kooi, M. Wuttig, *Adv. Mater.* **2020**, *32*, 1908302.
[44] T. Kirchartz, U. Rau, *Adv. Energy Mater.* **2018**, *8*, 1703385.
[45] G. C. Xing, N. Mathews, S. Y. Sun, S. S. Lim, Y. M. Lam, M. Gratzel, S. Mhaisalkar, T. C. Sum, *Science* **2013**, *342*, 344.
[46] S. D. Stranks, G. E. Eperon, G. Grancini, C. Menelaou, M. J. P. Alcocer, T. Leijtens, L. M. Herz, A. Petrozza, H. J. Snaith, *Science* **2013**, *342*, 341.
[47] L. Guarneri, S. Jakobs, A. v. Hoegen, S. Maier, O. Cojocaru-Mirédin, M. Raghuwanshi, M. Drögeler, C. Stampfer, R. P. S. M. Lobo, A. Piarristeguy, A. Pradel, M. Xu, M. Wuttig, *Adv. Mater.* **2021**, *33*, 2102356.
[48] S. Maier, S. Steinberg, Y. D. Cheng, C. F. Schön, M. Schumacher, R. Mazzarello, P. Golub, R. Nelson, O. Cojocaru-Miredin, J. Y. Raty, M. Wuttig, *Adv. Mater.* **2020**, *32*, 202005533.
[49] P. E. Blochl, *Phys. Rev. B* **1994**, *50*, 17953.
[50] X. Gonze, B. Amadon, P.-M. Anglade, J.-M. Beuken, F. Bottin, P. Boulanger, F. Bruneval, D. Calistae, R. Caracas, M. Coté, T. Deutsch, L. Genovese, P. Ghosez, M. Giantomassi, S. Goedecker, D. R. Haman, P. Hermet, F. Jollet, G. Jomard, S. Leroux, M. Mancini, S. Mazevet, M. J. T. Oliveira, G. Onida, Y. Pouillon, T. Rangel, G.-M. Rignanese, D. Sangalli, R. Shaltaf, M. Torrent, M. J. Verstraete, G. Zerah, J. W. Zwanziger, *Comput. Phys. Commun.* **2009**, *180*, 2582.
[51] M. Torrent, F. Jollet, F. Bottin, G. Zerah, X. Gonze, *Comput. Mater. Sci.* **2008**, *42*, 337.
[52] G. Kresse, M. Marsman, J. Furthmüller, *Vienna Ab Initio Simulation Package (VASP), The Guide*, Computational Materials Physics, Faculty of Physics, Universität Wien, Vienna, Austria **2014**.
[53] G. Kresse, J. Furthmüller, *Phys. Rev. B: Condens. Matter Mater. Phys.* **1996**, *54*, 11169.

© 2021 The Authors. Advanced Functional Materials published by Wiley-VCH GmbH

[54] G. Kresse, J. Furthmuller, *Comput. Mater. Sci.* **1996**, *6*, 15.
[55] G. Kresse, J. Hafner, *Phys. Rev. B: Condens. Matter Mater. Phys.* **1993**, *47*, 558.
[56] G. Kresse, D. Joubert, *Phys. Rev. B: Condens. Matter Mater. Phys.* **1999**, *59*, 1758.
[57] J. Sun, A. Ruzsinszky, J. P. Perdew, *Phys. Rev. Lett.* **2015**, *115*, 036402.
[58] E. B. Isaacs, C. Wolverton, *Phys. Rev. Mater.* **2018**, *2*, 063801.
[59] M. Bokdam, J. Lahnsteiner, B. Ramberger, T. Schaefer, G. Kresse, *Phys. Rev. Lett.* **2017**, *119*, 145501.
[60] S. Baroni, R. Resta, *Phys. Rev. B* **1986**, *33*, 7017.
[61] X. Gonze, *Phys. Rev. A* **1995**, *52*, 1096.
[62] X. Gonze, *Phys. Rev. A* **1995**, *52*, 1086.
[63] A. V. Krukau, O. A. Vydrov, A. F. Izmaylov, G. E. Scuseria, *J. Chem. Phys.* **2006**, *125*, 224106.
[64] R. F. W. Bader, M. E. Stephens, *J. Am. Chem. Soc.* **1975**, *97*, 7391.
[65] M. Yu, D. R. Trinkle, *J. Chem. Phys.* **2011**, *134*, 064111.
[66] X. Fradera, M. A. Austen, R. F. W. Bader, *J. Phys. Chem. A* **1999**, *103*, 304.
[67] M. Kohout, *DGrid, Version 4.7*, Springer, Dresden, Germany **2019**.
[68] J. P. Perdew, K. Burke, M. Ernzerhof, *Phys. Rev. Lett.* **1996**, *77*, 3865.

© 2021 The Authors. Advanced Functional Materials published by Wiley-VCH GmbH